

## **DESIGN OF ALTERNATIVE BINDERS FOR HARD MATERIALS**

M. de Nicolás <sup>1\*</sup>, H. Besharatloo <sup>2,3</sup>, P. Alvaredo <sup>1</sup>, J. J. Roa <sup>2,3</sup>, L. Llanes <sup>2,3</sup>, E. Gordo <sup>1</sup>

<sup>1</sup> GTP – Department of Materials Science and Engineering, IAAB, Universidad Carlos III de Madrid, 28911 Leganés, Madrid, Spain

<sup>2</sup> CIEFMA – Department of Materials Science and Metallurgical Engineering, Universitat Politècnica de Catalunya - BarcelonaTech, 08019 Barcelona, Spain

<sup>3</sup> Centre for Research in Multiscale Engineering of Barcelona, Universitat Politècnica de Catalunya - BarcelonaTech, 08019 Barcelona, Spain

\* Corresponding author, e-mail: [mnicolas@ing.uc3m.es](mailto:mnicolas@ing.uc3m.es)

## **Abstract**

In the last years, a special interest has emerged towards the total or partial substitution of traditional cemented carbides composing elements. In this study, a systematic methodology is presented and used to design iron-based binders for WC and Ti(C,N) ceramic phases. First, metal alloy phase diagrams were simulated by means of Thermo-Calc® software, combining several alloying elements (Ni, Al, Cr, Mo and C) to fulfil the following criteria: provide high corrosion resistance, least number of phases present at room temperature and solidus-liquidus temperatures below 1500 °C. Two final compositions were chosen: Fe15Ni10Cr and Fe15Cr10Al. Next step is to validate the critical temperatures by means of differential thermal analysis tests and, finally, high-temperature wetting experiments were conducted to measure the contact angle between molten metal and ceramic phases. Resultant metal-ceramic region was studied by means of field emission scanning electron microscopy, energy dispersive X-ray spectroscopy and nanoindentation techniques. As a proof of concept, samples with 80 vol. % of Ti(C,N) and WC ceramic phases were prepared for a basic characterisation. Both ceramic reinforcements were compared, and the presented methodology could satisfactorily be validated as a design procedure of alternative binders for hard materials.

**Keywords:** Cermets; Ti(C,N); Alternative binders; Thermodynamic simulation; Wettability

## 1. Introduction

Cemented carbides (WC-Co) have been the undeniable masters in the cutting tool field for almost over a century. The magnificent relationship between ceramic and metallic phases enables the configuration of hard and tough composite materials with high carbide contents and homogeneous microstructures. Nevertheless, in the last years both industry and scientific community have been seeking for alternative materials that can substitute the cobalt binder of hardmetals and, furthermore, the ceramic phase, due to economic and health reasons [1,2]. On one hand, ammonium paratungstate, the raw material from which WC is obtained, and Co have reported high and fluctuating market prices in the last two decades [3,4]. In 2011, the European Commission included Co and W in the European list of critical raw materials, renewing their membership in 2014 and 2017 subsequent lists [5–7]. On the other hand, recent investigations have demonstrated the toxicity of Co and its hazardous combination with WC for human health [8]. These substances have been included in REACH (EU) and NTP (US) programmes [9,10].

Regarding substitution of the Co binder, iron alloys have arisen as excellent candidates. Iron is an abundant element on the Earth's surface, which translates into a relatively low price. In addition, it is non-toxic and can be heat-treated to adjust the material final properties for the desired application [11,12].

Among possible substitutes for WC phase, titanium carbonitride, Ti(C,N), counts with high hardness and wear resistance, chemical stability and corrosion resistance, paramount properties for cutting tool applications [13]. One main drawback of this ceramic material is the lower wettability with the metal phase, especially with iron-based binders. This property is fundamental for liquid phase sintering and densification of the composite material during this stage. The problem has been overcome by addition of secondary carbides, such as Mo<sub>2</sub>C [14], or other alloying elements, like Ni [15,16]. Recent investigations have demonstrated that processing of Ti(C,N) with an FeNi alloy by powder metallurgy results in fully-dense cermets with final properties comparable to some cemented carbides [17,18]. Moreover, addition of a conservative

amount of extra carbon has shown to play a dramatic role during the sintering stage, by lowering solidus-liquidus temperatures and improving densification [19–21].

Although many investigations are being carried out in this area, a perfect cemented-carbide competitor has not yet been found, and this process is tough and time-consuming. The objective of this study is to present a flexible and systematic methodology for the design of hard materials, with which to find the optimum metal-ceramic combination. In particular, in this research, iron-based binders were combined with WC and Ti(C,N), respectively. The method consists of three steps:

- **Step 1: Thermodynamic simulation of phase diagrams.** Calculation of metal alloys phase diagrams and their combination with ceramic phases by means of Thermo-Calc® software. This CALculation of PHase Diagrams (CALPHAD) approach has proven to be not only very powerful but also extremely successful for developing cemented carbides since its pioneering introduction by KTH research groups in the 80s and the 90s (e.g. Refs. [22–25]) until recent years, when it has become a mandatory tool for such purpose (e.g. Refs. [26–33]). In this study, it was implemented by taking into consideration specific criteria: (a) provide high corrosion resistance, (b) closeness to a plain two-phase ceramic-metal microstructure, with the least number of phases present at room temperature, and (c) solidus-liquidus temperatures below 1500 °C, in order to approach an industrial sintering cycle. Ni, Al, Cr, Mo and C were selected as alloying elements attending to their properties, such as improvement of oxidation (Cr [34], Al [35–37]), wear (Al [38]) and corrosion resistance (Ni [34,39,40], Cr [33,40,41], Al [42]). Furthermore, it was also sought to enhance the metal-ceramic wetting behaviour (Ni [16], Mo [39], Cr [43]) and lower solidus-liquidus temperatures (C [16,19,20]), which will aid densification of the samples during sintering. Selected binder configurations were then combined with 80 vol. % of Ti(C,N) and WC, respectively, for simulation of composite materials phase diagrams.
- **Step 2: Validation of thermodynamic simulation.** This task was accomplished by means of two techniques: Differential Thermal Analysis-Thermogravimetric (DTA-TG), to check

the liquidus temperatures predicted by Thermo-Calc®, and high-temperature wetting experiments, to measure the contact angle between molten metal and ceramic phases [16,44,45]. The obtained metal-ceramic region was studied by FESEM (Field Emission Scanning Electron Microscopy), EDX (Energy Dispersive X-Ray), AFM (Atomic Force Microscopy) and nanoindentation techniques.

- **Step 3: Processing of hard materials.** Finally, samples with 80 vol. % of Ti(C,N) and WC ceramic phases were prepared by conventional powder metallurgy for a basic characterisation to validate the methodology and compare both ceramic reinforcements. Raw powders were wet milled in isopropyl alcohol for 12 h, dried in a rotary evaporator, pressed uniaxially and sintered in a high-vacuum furnace. A basic characterization of the final samples was done in terms of their density and microstructure (FESEM).

Both *Experimental procedure* (Section 2) and *Results and discussion* (Section 3) parts will be divided into these three steps, for easiness of the reader to follow the proposed systematic methodology.

## **2. Experimental procedure**

### **2.1. Thermodynamic simulation of phase diagrams**

Phase diagrams of different binders and their combination with Ti(C,N) and WC were simulated with Thermo-Calc® software, using TCFE7 database. Theoretical densities of the elements were used to configure the different studied materials. Effectiveness of the method and database employed were validated by simulating standardized WC-Co diagrams [3,34].

### **2.2. Validation of thermodynamic simulation**

DTA-TG tests were carried out to validate the phase diagrams of the chosen binder compositions, Fe15Ni10Cr and Fe15Cr10Al. As-received metal commercial powders, with no C addition, were blended in a Turbula® multidirectional mixer for 4 h. Then, they were compacted in a uniaxial press at 600 MPa, and sintered in a high-vacuum furnace ( $10^{-5}$  mbar) at 1450 °C for 1 h, to allow diffusion of the elements and formation of the alloy. Two samples were studied by DTA-TG (SETSYS Evolution 18, Bonsai Advanced Technologies) up to 1600 °C at 20 °C/min in an Ar atmosphere: a blended-powder agglomerate and a sintered alloy bulk, to study both the sintering behaviour of raw powders and the alloys critical temperatures, respectively.

Contact angle experiments were conducted to study the worst-case wettability scenarios between metal alloys without extra C and binderless Ti(C,N) ceramic substrates – as it is the ceramic material with more reported wettability problems – following the procedure described in Ref. [44]. Titanium carbonitride substrates were sintered by Spark Plasma Sintering (SPS, 1900 °C – 100 °C/min – 70 MPa), achieving a final relative density of 99.5 %. A bulk of each pre-sintered alloy, with no C addition, was mounted on top of the polished surface of a Ti(C,N) substrate, and the assembly was inserted in a tubular furnace under an Ar atmosphere. Temperature was risen up to 1600-1650 °C (depending on the composition) at different heating rates, while an externally adapted camera to one of the furnace ends recorded the formation and evolution of the metal drop

on the ceramic substrate. After cooling, the sample was transversally cut and embedded in conductive resin. Samples were prepared for superficial characterization by polishing with diamond paste down to 3  $\mu\text{m}$ , finishing with a colloidal  $\text{Al}_2\text{O}_3$  (alumina) step to release any work-hardening effects in the metal phase from the polishing stage. The two-phase metal/ceramic region was characterized by different techniques. Its microstructure and composition were studied by FESEM-EDX (FEI Teneo, Philips), with the performance of mappings. Atomic Force Microscopy (AFM) was employed to further characterize this zone and assess height difference between both phases, with Dimension 3100 equipment (VEECO). The obtained images were subsequently treated using the software WSXM® [46]. Nanoindentations at 1000 nm of maximum penetration depth ( $h$ ) were done at different areas of the contact angle cross-section. A Nanoindenter XP (MTS) unit was used, equipped with a continuous stiffness measurement (CSM) module, which enabled a dynamic determination of hardness ( $H$ ) and elastic modulus ( $E$ ) during the completion of the test. A Berkovich tip was employed to implement the test, which was carefully calibrated with fused silica as a standard sample, with known Young's modulus of 72 GPa. An array of nine (3x3) nanoindentations was performed at single-phase (ceramic and metal) and two-phase (ceramic/metal) regions, respectively. A constant distance of 50  $\mu\text{m}$  between imprints was set to avoid any overlapping effect of plastic deformation fields. The obtained data were analysed with Oliver and Pharr method [47,48]. A strain rate of  $0.05 \text{ s}^{-1}$  and a constant Poisson ratio of 0.3 were established. Residual imprints were observed by FESEM (Jeol 71000F).

### 2.3. Processing of hard materials

As-received commercial powders used in this study, as well as their characteristics, are listed in **Table 1**. Density of the powders was measured with an Accupyc He Multipycnometer (Micrometrics, USA). Powders size and PEG molecular weight were provided by each manufacturer.

Ceramic and metal powders were blended in 80 and 20 vol. %, respectively, with the compositions collected in **Table 2**. These volume percentages correspond to a 10-11 wt. % of Co in a regular cemented carbide. Extra carbon was added in 1 wt. % with respect to the metal matrix, to improve the sintering behaviour of the materials (lowering of solidus and liquidus temperatures) and compensate C loss during milling. Two methods were used to compare the processed hard materials:

- **M1 – Binder comparison (Ti(C,N)).** First, each of the two chosen binder alloys were mixed with Ti(C,N), to compare the effect of binder composition on the final composite material. Powders were blended in a Turbula® multidirectional mixer for 1 h prior to the milling step. Blends were milled in isopropyl alcohol (2-propanol) at 120 rpm for 12 h in a planetary mill (Fritsch Pulverisette), using stainless-steel vessels and balls. A 2 wt. % of polyethylene glycol (PEG) was added as pressing aid. After milling, mixtures were dried in a rotary evaporator.
- **M2 – Carbide comparison (Fe15Ni10Cr).** Then, as it will be explained in *Results* section, alloy Fe15Ni10Cr was selected and processed with Ti(C,N), on one hand, and WC, on the other hand, to compare both ceramic materials.

The obtained ceramic-metal powders were observed by Scanning Electron Microscopy (SEM) with an XL-30 microscope (Philips, Netherlands). All powders were uniaxially pressed at 600 MPa and sintered in a high-vacuum furnace ( $10^{-5}$  mbar) with the following cycle: 500 °C – 30 min, 800 °C – 30 min, 1450 °C – 2 h. Green and sintered samples densities were calculated from dimensions and mass. Relative density values were calculated as a function of theoretical density, determined by the rule of mixtures. A basic characterization of the sintered samples was done, studying their microstructure by FESEM with FEI Teneo microscope. Sample surfaces were prepared in a similar way to contact angle ones, but using 1 µm diamond paste as the last polishing step, and colloidal SiO<sub>2</sub> instead of alumina.



### 3. Results and discussion

#### 3.1. Binder and composite material design by thermodynamic simulation

For the **binder design**, binary phase diagrams of Fe with the rest of alloying elements were simulated, in order to have a general idea of the optimum content of each element. **Figure 1** shows the binary phase diagrams for: Fe-Ni, Fe-Cr, Fe-Al and Fe-Mo. The well-known Fe-C diagram is not shown for simplicity. As it can be appreciated, a small addition of Mo may rapidly result in precipitation of undesirable phases, like the thermally unstable intermetallic  $\text{Fe}_2\text{Mo}$  or laves phase ( $\lambda$ ) [49]. For this reason, and after checking the same result when combining Fe-Mo with a third alloying element, molybdenum was discarded from this study.

Next step consisted on the configuration of pseudo-binary phase diagrams, Fe-A-B, where A and B represent different alloying elements. In doing so, Fe-A composition was fixed, and the X wt. % addition of element B was studied by phase diagram simulation. Once the ternary alloy compositions were selected, their evolution with temperature as a function of carbon content was also simulated. These diagrams were built to confirm the fact that carbon lowers both solidus and liquidus temperatures of these types of systems, as stated in previous studies [16,19]. Moreover, they also gave information about the maximum limit of C addition, or how the materials would be affected from a possible dissolution of C from the ceramic phase or loss of this element during sintering. **Figure 2** displays pseudo-binary phase diagrams (left): Fe15Ni-XCr, where a 10 wt. % of Cr was chosen so that no  $\sigma$ -phase precipitation occurred, and Fe15Cr-XAl, with an election of 10 wt. % of Al, to be conservative. It is worth to point that higher Al contents were simulated but it was observed that, when combining the binder with Ti(C,N), large volume amounts of AlN were formed. Solidus temperature ( $T_{\text{solidus}}$ ) is highlighted with a bold green line, indicating the temperature above which liquid phase sintering can be performed. Graphite precipitation, appearing in the diagrams as a function of C mass percent, is indicated with a bold grey line. It can be appreciated that the second composition has higher solidus and liquidus temperatures,

which may be translated into worse sintering and densification behaviours at the limit temperature of 1500 °C.

Once the binder compositions were decided, hard phase was included in the simulation and diagrams were plotted as a function of C content, as shown in **Figure 3**. **Table 3** collects the nominal or theoretical C content of the studied composite materials, indicated by dashed blue lines in the diagrams of **Figure 3**. For Ti(C,N) simulation, simple microstructures are obtained at nominal C content, with some  $M_{23}C_6$  Cr-carbide precipitation in the FeNiCr case, and slight precipitation of aluminium nitride (less than 2 vol. %) for FeCrAl binder. In WC diagrams, theoretical C compositions show the presence of eta phase ( $\eta$ ,  $M_6C$ ), which will be solved by adding graphite to reach the optimum C-window (highlighted in blue), where only a slight amount of  $M_7C_3$  carbide is predicted to precipitate. Both alloys, combined with Ti(C,N) and WC, achieve solidus temperatures below 1500 °C, as well as containing elements that provide corrosion resistance and leading to a simple microstructure, thus meeting the established criteria for material selection.

### 3.2. Binder simulation validation and wettability study

#### 3.2.1. Thermo-Calc® binder phase diagram validation by DTA-TG analysis

Once the alternative binder configurations were selected, DTA-TG tests were carried out to blended-powder agglomerates and sintered-alloy bulks, without carbon addition, to validate liquid phase formation simulated by Thermo-Calc® with respect to C content (**Figure 2**). **Figure 4** and **Table 4** show the correlation between simulated (left) and experimental (right) data for FeNiCr (top) and FeCrAl (bottom) alloys.

For both compositions, it can be appreciated that powder-blends and sintered-bulks liquidus temperatures coincide. This result may indicate maintenance of nominal content of the elements after sintering. Nevertheless, these experimental liquidus temperatures are higher than the ones

predicted by Thermo-Calc® using TCFE7 database; in particular, a difference of 15 °C is found for Fe15Ni10Cr alloy, and 30 °C for Fe15Cr10Al composition. Moreover, it can be appreciated that, after the sintering, oxidation is avoided, as shown by the TG curves. Powder agglomerates of the raw powders gain mass, corresponding to oxygen acquired in the heating stage. Contrarily, sintered bulks do not experience this mass increment, as the solid-solution alloys tend to be more chemically stable and less reactive. It is also remarkable to note that FeCrAl agglomerate gains more mass during the heating than FeNiCr, which may mean that it will tend to oxidize more when sintered.

### 3.2.2. Wettability studies: contact angle tests

As explained in the *Experimental procedure* (Section 2), final validation stage corresponded to the performance of high-temperature wettability studies by means of contact angle tests. In doing so, a pre-sintered bulk of the chosen binder compositions, using no C addition, was placed on top of a Ti(C,N) substrate, to study the wettability worst-case scenario, regarding the ceramic material and no-graphitic sintering aid.

For **Fe15Ni10Cr-Ti(C,N)**, contact angle test revealed that this metallic composition could form a droplet on the ceramic substrate and wet its surface. **Figure 5** displays three pictures taken by the equipment adapted camera at 1440, 1523 and 1590 °C, showing the initial FeNiCr bulk on top of the Ti(C,N) substrate, drop formation and its evolution at the end of the heating ramp, respectively. The results match the DTA data, where the metal liquid-phase formation occurred at 1492 °C.

**Figure 6** shows the contact angle cross-section characterized by FESEM. A value of 26 ° between the droplet and substrate surfaces was measured, as well as a mean penetration depth of  $336 \pm 16$  μm of liquid metal into the Ti(C,N) substrate. These results show the good wettability of FeNiCr alloy on the ceramic material, with high diffusion of the elements along the whole assembly and dissolution of Ti(C,N) particles, which enable the metal penetration into the substrate, translated

into a decrease in the contact angle. Carbide re-precipitation could be observed in the metal drop area, pointed by light-blue arrows in **Figure 6** (left). This carbide-dissolving ability of the metal binder was observed in wettability studies carried out for a Fe<sub>15</sub>Ni-Ti(C,N) system [16]. The two-phase metal/ceramic region, formed between the metal-drop and Ti(C,N) substrate single phases, can be considered as a recreation or model of the bulk hard material (cermet) that can be obtained after powder metallurgy processing.

**Figure 7** displays a mapping analysis by FESEM/EDX, where a section of FeNiCr-Ti(C,N) contact angle was analyzed. Elements volume percentage and distribution can be appreciated: Ti, C and N were concentrated at the substrate region and carbides precipitated in the metal area, whereas Fe, Ni and Cr appear mainly in the metal region.

EDX analysis were done on the precipitated carbides at metal-drop area to have a more accurate idea of their composition. **Figure 8** shows the spots and binder area where EDX analysis were carried out, whose results are given in **Table 5** (at. %). These carbides seem to have two essential compositions: TiC (Spot 1, [16]) and M<sub>23</sub>C<sub>6</sub>/M<sub>7</sub>C<sub>3</sub>-type carbides (Spots 2 and 3), whose formation was already predicted in the hard material phase diagram (**Figure 3**). This latter type of carbides are known to be appearing at the grain boundaries of the metallic phase [50]. An interesting fact was the similar element content of the binder and the MC-type carbides, where the latter ones form from the former by diffusion of a large amount of C and slight of Ti.

AFM was also employed to characterize the two-phase cermet area and assess the height difference between metallic and ceramic phases. AFM 3D-view and topography (left and centre images in **Figure 9**, respectively) show, in detail, the contact angle microstructure, with the metal region positioned on the left side and Ti(C,N) area, on the right. Furthermore, the total height difference observed in the AFM profile (right image in **Figure 9**) between binder and carbide single-phases is, approximately, 684  $\mu\text{m}$  ( $h_{\text{single-phase}}$ ). This difference is due to the softer response of the metal to polishing from surface preparation stage. The metal/ceramic height difference at the bi-phasic zone was of 240  $\mu\text{m}$  ( $h_{\text{two-phase}}$ ), lower than the total metal-ceramic value because of the wear protection offered by the embedded Ti(C,N) particles. Nanoindentation tests were

conducted at the metal, two-phase (cermet) and ceramic regions. The indentation depth employed, 1000 nm, was higher than  $h_{\text{single-phase}}$  and  $h_{\text{two-phase}}$ , in order to avoid any scale effect that can induce modifications in the mechanical properties. As the carbide-metal height difference in the two-phase region is around 240  $\mu\text{m}$ , this result validates the use of the employed penetration depth to characterize this cermet area.

**Figure 10** collects a stitching of FESEM images of the contact angle cross-section, as well as the residual nanoindentation imprints, indicating the three existing and tested areas:

- 1) Metal or binder single-phase, with a centre image of the nine nanoindentations performed, zooming in one of them to point out the existence of parallel lines with an approximate angle of 65 °. At the used microscopic scale, these features show some plastic deformation, i.e. slip traces or mechanical twinning. Hypothetically, if observed at the nanometric length scale, these lines may mean dislocations pile-up and phase transformation of austenite into martensite [51].
- 2) Metal/ceramic bi-phasic region (cermet), where a combination of ductile-brittle response to deformation takes place, a model of the behaviour of this type of composite materials. Here, the residual imprint detail shows intergranular cracks at the Ti(C,N) particle, indicated by yellow arrows, and ductile deformation with stacking of planes in the binder area, pointed out in dark blue colour.
- 3) Ceramic single-phase, where brittle fracture in the shape of intergranular cracks (yellow arrows) and particle-particle separation at interfaces (pink arrows) was observed, as there was no metal phase to absorb the deformation induced by the indentation process in a ductile way.

Hardness results of the nanoindentation test, expressed in GPa, are collected in **Table 6**, obtaining similar values and the same trend than for micromechanical testing of Fe15Ni-Ti(C,N) cermets performed in a recent investigation [52]. Large scatter observed in region-2 hardness is related to the dependence on ceramic-metal area covered by each imprint.

For **Fe15Cr10Al-Ti(C,N)** system, contact angle test was carried out 50 °C higher than for the first composition, as simulated and DTA (sintered bulk) liquid-formation temperatures were higher for this composition. As it can be appreciated in **Figure 11**, the metal sample did not reach its melting point, probably due to oxidation that this particular alloy composition may be experiencing [36], and a contact angle could not be measured.

After performance of Steps 1 and 2, it could be stated that Fe15Ni10Cr matrix would have better sinterability with Ti(C,N) than composition Fe15Cr10Al. Nevertheless, both of them were processed by powder metallurgy to achieve a final composite material and proof these concepts.

### **3.3. Composite material processing and final sintered materials characterization**

#### **3.3.1. M1, binder comparison: FeNiCr-Ti(C,N) and FeCrAl-Ti(C,N)**

This first hard material comparison method was employed as methodology proof of concept, combining the two selected binder compositions, Fe15Ni10Cr and Fe15Cr10Al, with Ti(C,N).

**Figure 12** shows the ceramic-metal mixture powders for both compositions, after being wet milled and dried in a rotary evaporator, where agglomerates of the different phases were obtained.

**Figure 13** displays the FESEM microstructures of final sintered materials. As it can be appreciated, FeNiCr binder combined with Ti(C,N) achieves a homogeneous and bi-phasic microstructure, which resembles the traditional cemented carbides one. Microporosity inside some carbides could be observed, which may be due to incomplete carbide-carbide sintering, or to nitrogen elimination during the sintering stage, a common problem when vacuum-sintering cermet materials [53]. On the other hand, FeCrAl-Ti(C,N) sample showed a heterogeneous and very porous microstructure, with low binder wettability and agglomeration of carbide particles. These findings matched the measurements of sintered relative density, included in **Table 7**.

From microstructure and density results, it could be stated that FeNiCr could achieve a densified and homogeneous final material, opposite to FeCrAl binder. This dissimilar behaviour was

already predicted in the previous steps: for FeCrAl, higher solidus-liquidus temperatures were predicted (**Figure 2** and **Figure 3**), higher oxidation was observed in DTA-TG results of blended-raw powder agglomerates (**Figure 4**) and no metal drop formed during the wettability test (**Figure 11**). Then, effectiveness of the developed methodology is confirmed.

### 3.3.2. M2, carbide comparison: FeNiCr-Ti(C,N) and FeNiCr-WC

As FeNiCr alloy shows the best properties when combined with Ti(C,N), this was the selected binder to compare the two carbide phases, Ti(C,N) and WC. **Figure 14** shows SEM images of powder agglomerates obtained after milling.

**Figure 15** and **Table 8** collect FESEM microstructures and green/sintered relative densities, respectively, of the studied materials. It can be observed that, in this first processing attempt, FeNiCr-WC showed good wettability, but a heterogeneous microstructure, with carbide agglomeration and binder pools (some of them highlighted by white-dashed ellipses in the lower magnification image of **Figure 15**). A hypothesis is that the chosen sintering temperature (1450 °C) appears to be too high for FeNiCr-WC, as its solidus temperature is predicted to be between 1200 and 1300 °C (**Figure 3**). Future work will focus on the adjustment of its heating cycle and processing parameters.

#### **4. Conclusions**

This investigation develops a three-step flexible and systematic methodology for the design of alternative binders for hard materials. In particular, iron-based metal alloys are combined with Ti(C,N) and WC ceramic phases.

First step consisted on the design of binders and hard materials by phase-diagram simulation, employing Thermo-Calc® software tool. Two metallic compositions were selected, Fe15Ni10Cr and Fe15Cr10Al. Second stage of the process entailed the design validation by DTA-TG analysis and contact angle tests of the sintered alloys on a Ti(C,N) binderless substrate. The former tests showed correlation between simulated and experimental binder liquidus temperatures. High-temperature wetting experiments revealed the optimum behaviour of FeNiCr composition, unlike FeCrAl alloy. In the third step, hard materials were processed by conventional powder metallurgy, as a proof of concept for the presented methodology. Characterization results of the sintered samples confirmed that binder FeNiCr achieved well-densified and homogeneous materials, whereas FeCrAl composition lead to a porous microstructure with carbide agglomeration. Finally, FeNiCr binder was processed with WC to compare both ceramic materials, where good wettability of the binder, embedding the carbide particles, could be appreciated. Future work efforts will focus in the optimization of these first-approach processing parameters and hard materials microstructures.



## **Acknowledgements**

The current study was supported by the Spanish *Ministerio de Economía y Competitividad* through the project MAT2015-70780-C4-P and grant BES-2016-077340, and the Regional Government of Madrid through the program ADITIMAT, ref. S2018/NMT-4411. The authors would like to acknowledge the contribution of M. Campos for setting up milling conditions. J. J. Roa acknowledges the Serra Hunter programme of the *Generalitat de Catalunya*.

## References

- [1] V.K. Sarin, D. Mari, L. Llanes, C.E. Nebel, eds., *Comprehensive Hard Materials*, Volumes I-III, Elsevier, Oxford (UK), 2014.
- [2] G.S. Upadhyaya, *Cemented Tungsten Carbides: Production, Properties and Testing*, Noyes Publications, New Jersey (US), 1998.
- [3] S. Norgren, J. Garcia, A. Blomqvist, L. Yin, Trends in the P/M hard metal industry, *Int. J. Refract. Met. Hard Mater.* 48 (2015) 31–45. doi:10.1016/j.jirmhm.2014.07.007.
- [4] Historical Cobalt Prices and Price Chart, InfoMine. (n.d.). <http://www.infomine.com/investment/metal-prices/cobalt/all/> (accessed April 1, 2019).
- [5] European Commission, Communication from the Commission to the European Parliament, the Council, the European Economic and Social Committee and the Committee of the Regions - Tackling the Challenges in Commodity Markets and on Raw Materials, 2011.
- [6] European Commission, Report on Critical Raw Materials for the EU, 2014. doi:Ref. Ares(2015)1819595 - 29/04/2015.
- [7] European Commission, Communication from the Commission to the European Parliament, the Council, the European Economic and Social Committee and the Committee of the Regions on the 2017 list of Critical Raw Materials for the EU, 2017. <https://ec.europa.eu/transparency/regdoc/rep/1/2017/EN/COM-2017-490-F1-EN-MAIN-PART-1.PDF>.
- [8] S. Bastian, W. Busch, D. Kühnel, A. Springer, T. Meißner, R. Holke, S. Scholz, M. Iwe, W. Pompe, M. Gelinsky, A. Potthoff, V. Richter, C. Ikonomidou, K. Schirmer, Toxicity of tungsten carbide and cobalt-doped tungsten carbide nanoparticles in mammalian cells in vitro, *Environ. Health Perspect.* 117 (2009) 530–535. doi:10.1289/ehp.0800121.
- [9] EU Registration, Evaluation, Authorisation and Restriction of Chemical substances (REACH) programme, (n.d.). [https://ec.europa.eu/growth/sectors/chemicals/reach\\_en](https://ec.europa.eu/growth/sectors/chemicals/reach_en)

(accessed April 1, 2019).

- [10] US National Toxicology Program (NTP), (n.d.). <https://ntp.niehs.nih.gov/> (accessed April 1, 2019).
- [11] K. Aigner, W. Lengauer, P. Ettmayer, Interactions in iron-based cermet systems, *J. Alloys Compd.* 262–263 (1997) 486–491. doi:10.1016/S0925-8388(97)00360-5.
- [12] J.A. Canteli, J.L. Cantero, N.C. Marín, B. Gómez, E. Gordo, M.H. Miguélez, *Journal of Materials Processing Technology* Cutting performance of TiCN – HSS cermet in dry machining, 210 (2010) 122–128. doi:10.1016/j.jmatprotec.2009.08.003.
- [13] Y. Peng, H. Miao, Z. Peng, Development of TiCN-based cermets: Mechanical properties and wear mechanism, *Int. J. Refract. Met. Hard Mater.* 39 (2013) 78–89. doi:10.1016/j.ijrmhm.2012.07.001.
- [14] Z. Guo, J. Xiong, M. Yang, J. Wang, L. Sun, Y. Wu, J. Chen, S. Xiong, Microstructure and properties of Ti(C,N)–Mo<sub>2</sub>C–Fe cermets, *Int. J. Refract. Met. Hard Mater.* 27 (2009) 781–783. doi:10.1016/j.ijrmhm.2009.01.003.
- [15] H.-O. Andren, Microstructures of cemented carbides, *Mater. Des.* 22 (2001) 491–498. doi:10.1016/S0261-3069(01)00006-1.
- [16] P. Alvaredo, M. Dios, B. Ferrari, E. Gordo, Understanding of wetting and solubility behavior of Fe binder on Ti(C,N) cermets, *J. Alloys Compd.* 770 (2019) 17–25. doi:10.1016/j.jallcom.2018.07.243.
- [17] M. Dios, I. Kraveva, Z. González, P. Alvaredo, B. Ferrari, E. Gordo, R. Bermejo, Mechanical characterization of Ti(C,N)-based cermets fabricated through different colloidal processing routes, *J. Alloys Compd.* 732 (2018) 806–817. doi:10.1016/j.jallcom.2017.10.274.
- [18] M. Dios, Z. Gonzalez, P. Alvaredo, R. Bermejo, E. Gordo, B. Ferrari, Novel colloidal approach for the microstructural improvement in Ti(C,N)/FeNi cermets, *J. Alloys Compd.*

724 (2017) 327–338. doi:10.1016/j.jallcom.2017.07.034.

- [19] Y. Zhao, Y. Zheng, W. Zhou, J. Zhang, Q. Huang, W. Xiong, Effect of carbon addition on the densification behavior, microstructure evolution and mechanical properties of Ti(C, N)-based cermets, *Ceram. Int.* 42 (2016) 5487–5496. doi:10.1016/j.ceramint.2015.12.097.
- [20] P. Alvaredo, S.A. Tsipas, E. Gordo, Influence of carbon content on the sinterability of an FeCr matrix cermet reinforced with TiCN, *Int. J. Refract. Met. Hard Mater.* 36 (2013) 283–288. doi:10.1016/j.ijrmhm.2012.10.007.
- [21] P. Alvaredo, D. Mari, E. Gordo, High temperature transformations in a steel-TiCN cermet, *Int. J. Refract. Met. Hard Mater.* 41 (2013) 115–120. doi:10.1016/j.ijrmhm.2013.02.012.
- [22] A.F. Guillermet, An assessment of the Fe-Ni-W-C phase diagram, *Metallkunde.* 78 (1987) 165–170.
- [23] A.F. Guillermet, Use of phase diagram calculations in selecting the composition of Fe-Ni bonded WC tools, *Int. J. Refract. Hard Met.* 6 (1987) 24–27.
- [24] B. Uhrenius, Phase diagrams as a tool for production and development of cemented carbides and steels, *Powder Metall.* 35 (1992) 203–210. doi:10.1179/pom.1992.35.3.203.
- [25] B. Uhrenius, H. Pastor, E. Pauty, F.G. Cedex, On the composition of Fe-Ni-Co-WC-based cemented carbides, 15 (1997) 139–149. doi:https://doi.org/10.1016/S0263-4368(96)00023-6.
- [26] B. Kaplan, S. Norgren, M. Schwind, M. Selleby, Thermodynamic calculations and experimental verification in the WC–Co–Cr cemented carbide system, *Int. J. Refract. Hard Mater.* 48 (2015) 257–262. doi:10.1016/j.ijrmhm.2014.09.016.
- [27] E. Franco, C.E. Da Costa, S.A. Tsipas, E. Gordo, Cermets based on FeAl-NbC from composite powders: Design of composition and processing, *Int. J. Refract. Met. Hard Mater.* 48 (2015) 324–332. doi:10.1016/j.ijrmhm.2014.09.030.
- [28] W.D. Schubert, M. Fugger, B. Wittmann, R. Useldinger, Aspects of sintering of cemented

- carbides with Fe-based binders, *Int. J. Refract. Met. Hard Mater.* 49 (2015) 110–123. doi:10.1016/j.ijrmhm.2014.07.028.
- [29] P. Zhou, Y. Peng, C. Buchegger, Y. Du, W. Lengauer, Experimental investigation and thermodynamic assessment of the C–Co–Fe–Ni–W system, *Int. J. Refract. Met. Hard Mater.* 54 (2016) 60–69. doi:10.1016/j.ijrmhm.2015.07.021.
- [30] S.G. Huang, J. Vleugels, H. Mohrbacher, M. Woydt, Microstructure and mechanical properties of NbC matrix cermets using Ni containing metal binder, *Met. Powder Rep.* 71 (2016) 349–355. doi:10.1016/j.mprp.2016.05.009.
- [31] S. Norgren, J. García, On gradient formation in alternative binder cemented carbides, *Int. J. Refract. Met. Hard Mater.* 73 (2018) 106–110. doi:10.1016/J.IJRMHM.2018.01.024.
- [32] J.J. Pittari, H.A. Murdoch, S.M. Kilczewski, B.C. Hornbuckle, J.J. Swab, K.A. Darling, J.C. Wright, Sintering of tungsten carbide cermets with an iron-based ternary alloy binder: Processing and thermodynamic considerations, *Int. J. Refract. Met. Hard Mater.* 76 (2018) 1–11. doi:10.1016/j.ijrmhm.2018.05.008.
- [33] R. De Oro, A. Agna, U. Umbelino, W.-D. Schubert, Phase formation in cemented carbides prepared from WC and stainless steel powder – An experimental study combined with thermodynamic calculations, *Int. J. Refract. Metals Hard Mater.* 80 (2019) 225–237. doi:10.1016/j.ijrmhm.2019.01.012.
- [34] C.M. Fernandes, A.M.R. Senos, Cemented carbide phase diagrams: A review, *Int. J. Refract. Met. Hard Mater.* 29 (2011) 405–418. doi:10.1016/j.ijrmhm.2011.02.004.
- [35] R. Subramanian, J. Schneibel, FeAl–TiC and FeAl–WC composites—melt infiltration processing, microstructure and mechanical properties, *Mater. Sci. Eng. A.* 244 (1998) 103–112. doi:10.1016/S0921-5093(97)00833-2.
- [36] R. Furushima, K. Katou, K. Shimojima, H. Hosokawa, M. Mikami, A. Matsumoto, Effect of  $\eta$ -phase and FeAl composition on the mechanical properties of WC–FeAl composites,

- Intermetallics. 66 (2015) 120–126. doi:10.1016/j.intermet.2015.06.023.
- [37] M.S. Archana, V.V.S.S. Srikanth, S.V. Joshi, J. Joardar, Influence of applied pressure during field-assisted sintering of Ti(C,N)–WC–FeAl based nanocomposite, *Ceram. Int.* 41 (2015) 1986–1993. doi:10.1016/j.ceramint.2014.09.022.
- [38] R. Kant, U. Prakash, V. Agarwala, V.V. Satya Prasad, Microstructure and wear behaviour of FeAl-based composites containing in-situ carbides, *Bull. Mater. Sci.* 39 (2016) 1827–1834. doi:10.1007/s12034-016-1326-4.
- [39] Z. Zhao, J. Liu, H. Tang, X. Ma, W. Zhao, Effect of Mo addition on the microstructure and properties of WC–Ni–Fe hard alloys, *J. Alloys Compd.* 646 (2015) 155–160. doi:10.1016/j.jallcom.2015.05.277.
- [40] P.K. Samal, J.W. Newkirk, eds., *ASM Handbook, Volume 7: Powder Metallurgy*, ASM International, Ohio (US), 2015.
- [41] C.M. Fernandes, V. Popovich, M. Matos, A.M.R. Senos, M.T. Vieira, Carbide phases formed in WC–M (M = Fe/Ni/Cr) systems, *Ceram. Int.* 35 (2009) 369–372. doi:10.1016/j.ceramint.2007.11.001.
- [42] W.H. Haynes, ed., *CRC Handbook of Chemistry and Physics, 95th ed.*, Taylor & Francis Group, Boca Raton (US), 2014.
- [43] A.P. Umanskii, Titanium carbonitride composite with iron – chromium binder, *Powder Metall. Met. Ceram.* 40 (2001) 637–640. doi:https://doi.org/10.1023/A:1015248407568.
- [44] P. Alvaredo, J.J. Roa, E. Jimenez-Pique, L. Llanes, E. Gordo, Characterization of interfaces between TiCN and iron-base binders, *Int. J. Refract. Met. Hard Mater.* 2 (2016) 6–11. doi:10.1016/j.ijrmhm.2016.08.010.
- [45] I. Konyashin, A.A. Zaitsev, D. Sidorenko, E.A. Levashov, B. Ries, S.N. Konischev, M. Sorokin, A.A. Mazilkin, M. Herrmann, A. Kaiser, Wettability of tungsten carbide by liquid binders in WC–Co cemented carbides: Is it complete for all carbon contents?, *Int. J.*

- Refract. Met. Hard Mater. 62 (2017) 134–148. doi:10.1016/j.ijrmhm.2016.06.006.
- [46] J.M. Gómez-Rodríguez, I. Horcas, J. Gómez-Herrero, A.M. Baro, J. Colchero, R. Fernández, WSXM: A software for scanning probe microscopy and a tool for nanotechnology, *Rev. Sci. Instrum.* 78 (2007) 013705. doi:10.1063/1.2432410.
- [47] W.C. Oliver, G.M. Pharr, An improved technique for determining hardness and elastic modulus using load and displacement sensing indentation experiments, *J. Mater. Res.* 7 (1992) 1564–1583. doi:https://doi.org/10.1557/JMR.1992.1564.
- [48] W.C. Oliver, G.M. Pharr, Measurement of hardness and elastic modulus by instrumented indentation: Advances in understanding and refinements to methodology, *J. Mater. Res.* 19 (2004) 3–20. doi:10.1117/12.461379.
- [49] J. Pavlu, M. Sob, Ab initio study of C14 laves phases in Fe-based systems, *J. Min. Metall. Sect. B Metall.* 48 (2012) 395–401. doi:10.2298/JMMB120704050P.
- [50] H.U. Hong, B.S. Rho, S.W. Nam, Correlation of the M23C6 precipitation morphology with grain boundary characteristics in austenitic stainless steel, *Mater. Sci. Eng. A.* 318 (2001) 285–292. doi:10.1016/S0921-5093(01)01254-0.
- [51] I. Sapezanskaia, J.J. Roa, G. Fargas, M. Turon-Viñas, T. Trifonov, R. Kouitat Njiwa, A. Redjaïmia, A. Mateo, Deformation mechanisms induced by nanoindentation tests on a metastable austenitic stainless steel: A FIB/SIM investigation, *Mater. Charact.* 131 (2017) 253–260. doi:10.1016/j.matchar.2017.07.019.
- [52] H. Besharatloo, M. de Nicolás, J.J. Roa, M. Dios, A. Mateo, B. Ferrari, E. Gordo, L. Llanes, Assessment of mechanical properties at microstructural length scale of Ti(C,N)–FeNi ceramic-metal composites by means of massive nanoindentation and statistical analysis, *Ceram. Int.* 45 (2019) 20202–20210. doi:10.1016/j.ceramint.2019.06.292.
- [53] V. Schwarz, F. Scagnetto, W. Lengauer, Sintering of Ti(C,N)-WC/Mo<sub>2</sub>C-(Ta,Nb)C-Co/Ni cermets investigated by CO and N<sub>2</sub> outgassing, *Metals (Basel).* 9 (2019) 427.

doi:10.3390/met9040427.



## List of Figures

**Figure 1.** Thermo-Calc® binary phase diagrams: Fe-Ni, Fe-Cr, Fe-Al and Fe-Mo.

**Figure 2.** Thermo-Calc® pseudo-binary phase diagrams (left) and final-composition alloys as function of C content (right). Bold green and grey lines indicate  $T_{\text{solidus}}$  and graphite precipitation, respectively.

**Figure 3.** Hard material phase diagrams, combining 80 vol. % of Ti(C,N) (left) and WC (right) with the two selected binder compositions, Fe15Ni10Cr (top) and Fe15Cr10Al (bottom). Dashed blue lines indicate theoretical carbon content present in the hard materials with no C addition. Blue highlighted areas in WC diagrams indicate the optimum C-window.

**Figure 4.** Correlation between Fe15Ni10Cr (top) and Fe15Cr10Al (bottom) liquidus temperatures, from simulated phase diagrams (left) and DTA-TG analysis (right), without C addition.

**Figure 5.** Contact-angle adapted camera pictures taken at 1440, 1523 and 1590 °C, showing the metal drop formation and evolution for Fe15Ni10Cr-Ti(C,N) system.

**Figure 6.** FESEM images of FeNiCr-Ti(C,N) contact angle cross-section, with measurements of droplet-substrate angle (left) and metal penetration layer (right).

**Figure 7.** Mapping analysis of FeNiCr-Ti(C,N) metal/ceramic region showing elements distribution, where composition is expressed in volume %.

**Figure 8.** FESEM image of the binder region in FeNiCr-Ti(C,N) contact angle, where carbide re-precipitation was observed.

**Figure 9.** AFM 3D-view (left) and topographic (centre) images of FeNiCr-Ti(C,N) contact metal/ceramic region. Profile measurement (right) indicates the height difference between binder/carbide single-phase areas ( $h_{\text{single-phase}}$ ) and binder/carbide at the two-phase zone ( $h_{\text{two-phase}}$ ).

**Figure 10.** Image stitching of FeNiCr-Ti(C,N) contact angle (left), indicating the three areas (1-metal, 2-metal/ceramic, 3-ceramic) where residual nanoindentation imprints could be observed (centre), pointing out special features about each kind (right).

**Figure 11.** Fe<sub>10</sub>Cr<sub>10</sub>Al-Ti(C,N) contact-angle adapted camera pictures taken at different temperatures, showing the no-formation of the metal drop.

**Figure 12.** SEM images of FeNiCr-Ti(C,N) (left) and FeCrAl-Ti(C,N) (right) mixture powders.

**Figure 13.** FeNiCr-Ti(C,N) (top) and FeCrAl-Ti(C,N) (bottom) FESEM microstructures, at two different magnifications.

**Figure 14.** SEM images of FeNiCr-Ti(C,N) (left) and FeNiCr-WC (right) mixture powders.

**Figure 15.** FeNiCr-Ti(C,N) (top) and FeNiCr-WC (bottom) FESEM microstructures, at two different magnifications. White-dashed ellipses point out some of the binder pools in WC-FeNiCr composition.

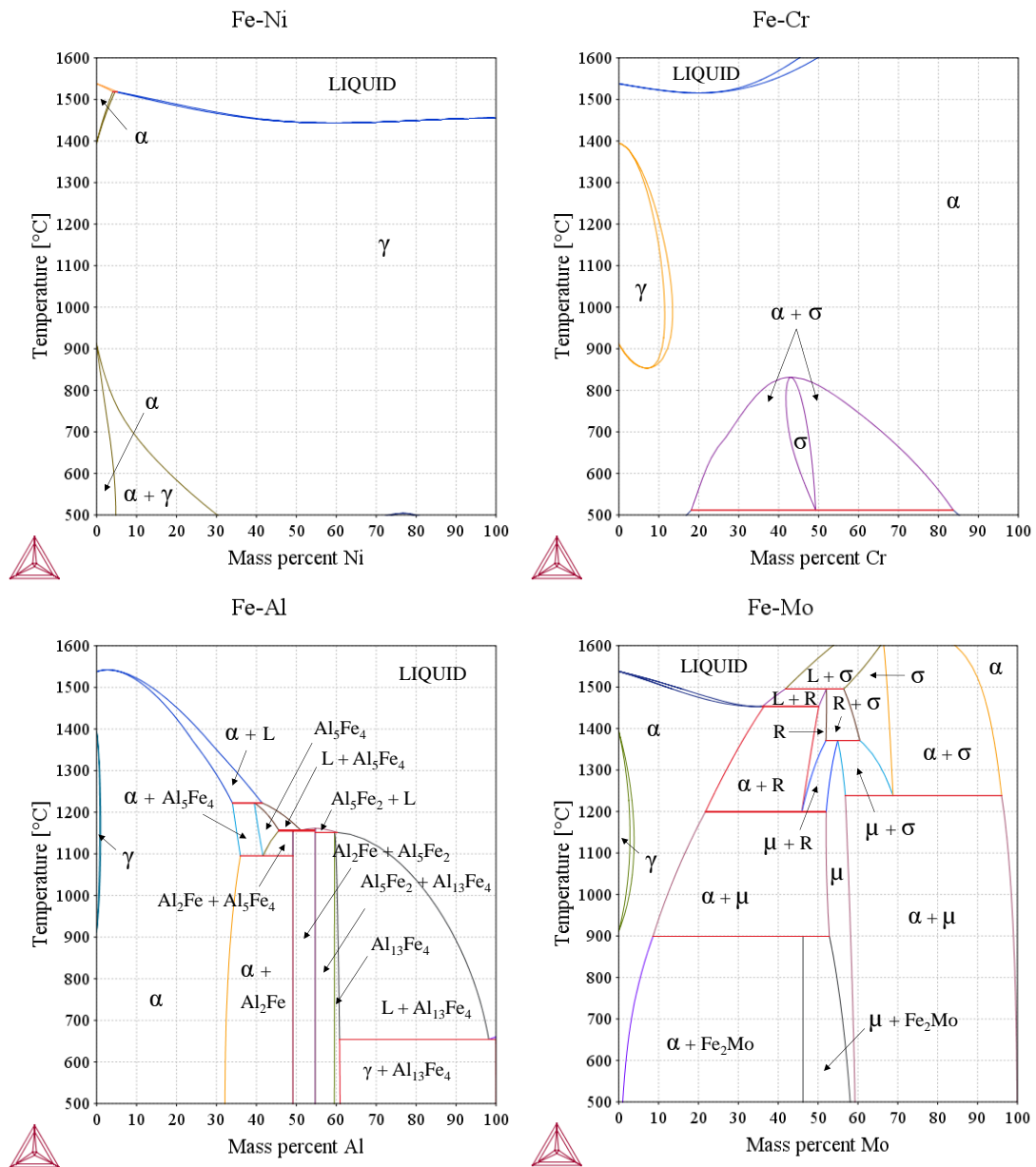


**Figure 1.** Thermo-Calc® binary phase diagrams: Fe-Ni, Fe-Cr, Fe-Al and Fe-Mo.

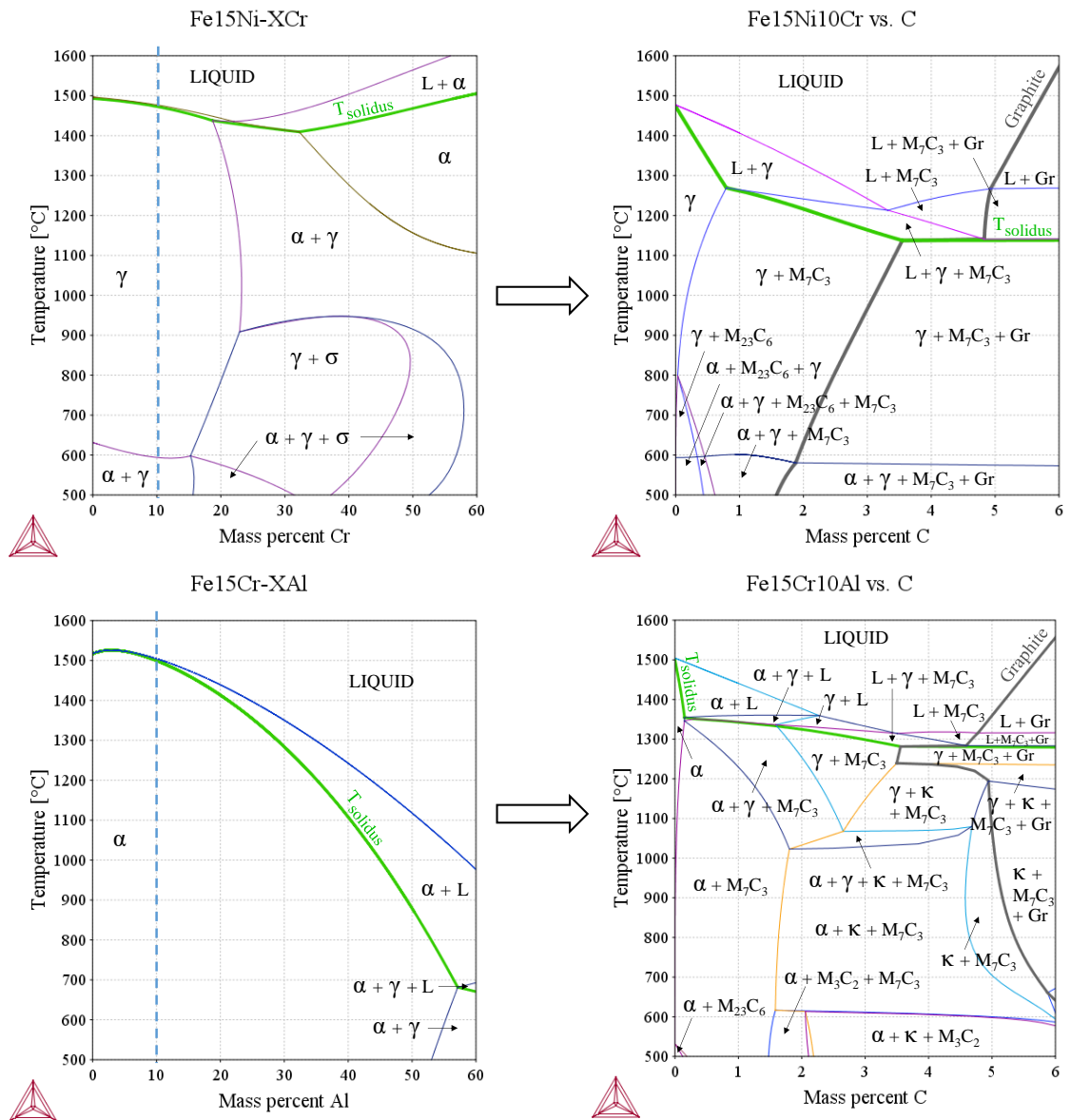


**Figure 2.** Thermo-Calc® pseudo-binary phase diagrams (left) and final-composition alloys as function of C content (right). Bold green and grey lines indicate  $T_{\text{solidus}}$  and graphite precipitation, respectively.

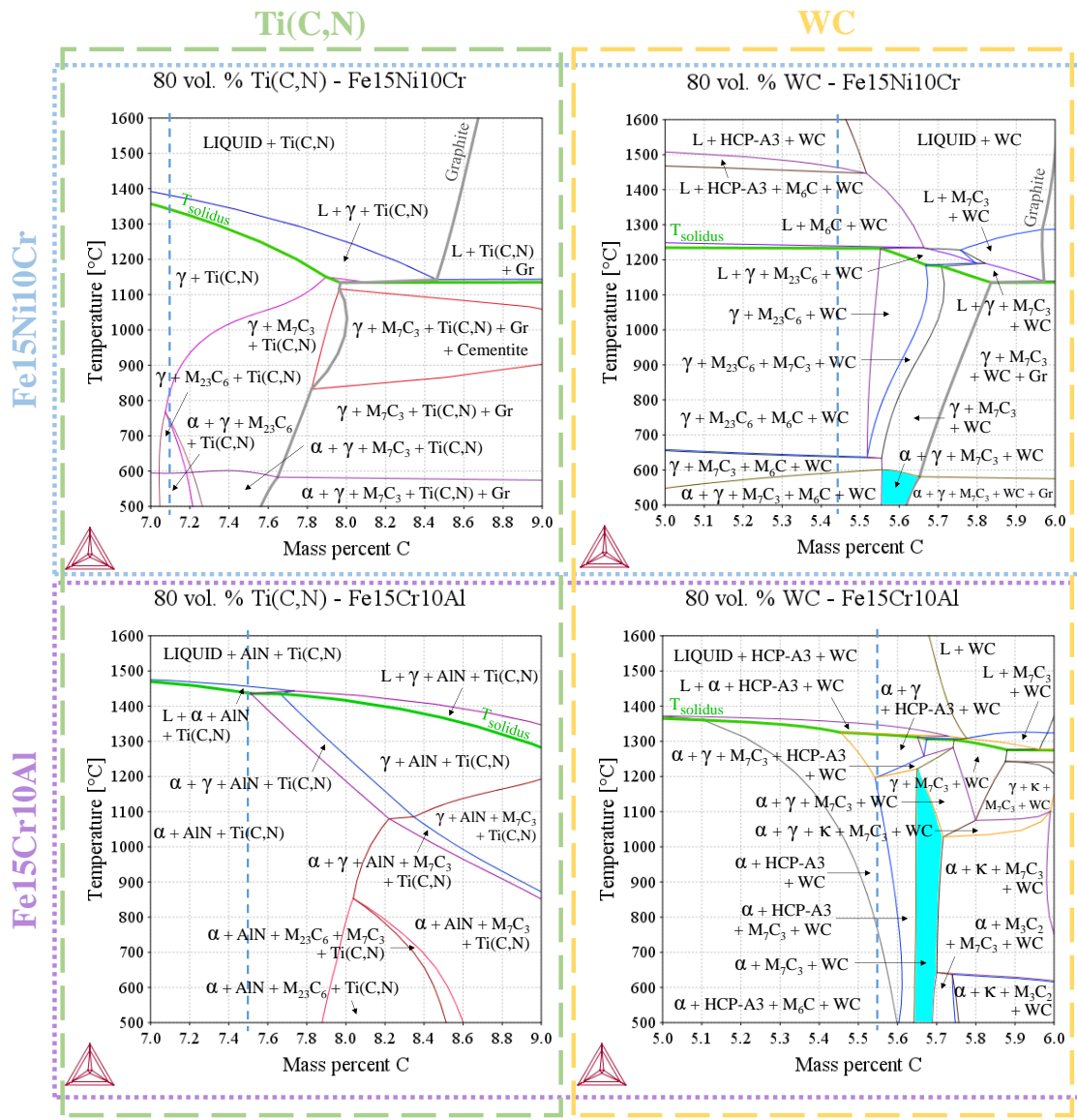


**Figure 3.** Hard material phase diagrams, combining 80 vol. % of Ti(C,N) (left) and WC (right) with the two selected binder compositions, Fe15Ni10Cr (top) and Fe15Cr10Al (bottom). Dashed blue lines indicate theoretical carbon content present in the hard materials with no C addition. Blue highlighted areas in WC diagrams indicate the optimum C-window.

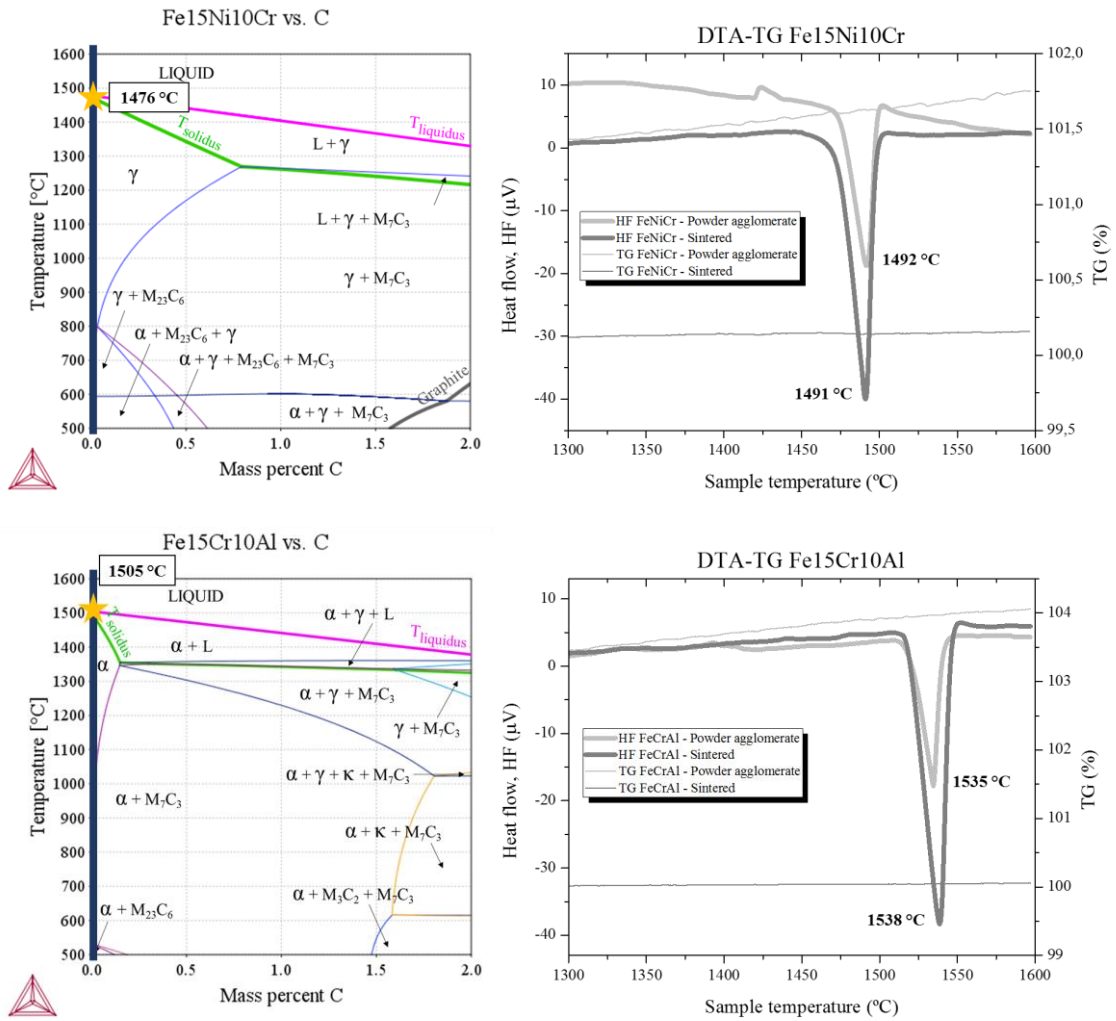


**Figure 4.** Correlation between Fe15Ni10Cr (top) and Fe15Cr10Al (bottom) liquidus temperatures, from simulated phase diagrams (left) and DTA-TG analysis (right), without C addition.



**Figure 5.** Contact-angle adapted camera pictures taken at 1440, 1523 and 1590 °C, showing the metal drop formation and evolution for Fe<sub>15</sub>Ni<sub>10</sub>Cr-Ti(C,N) system.

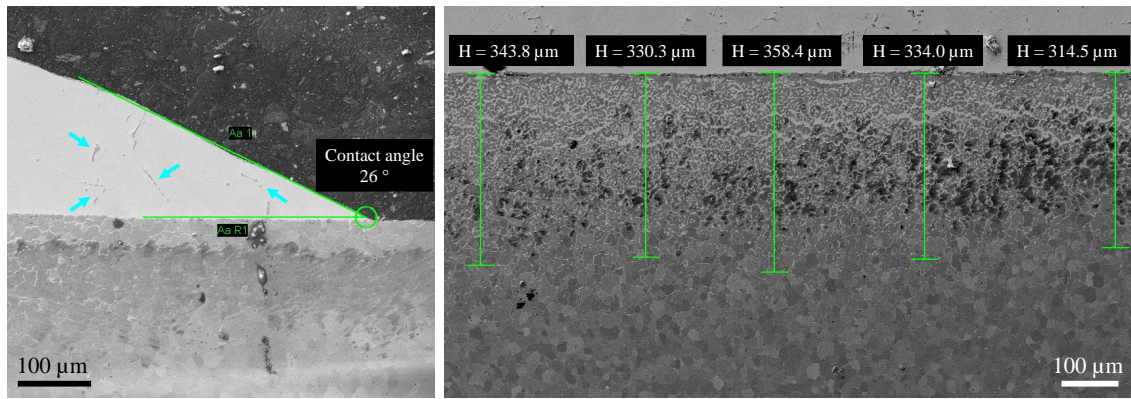


**Figure 6.** FESEM images of FeNiCr-Ti(C,N) contact angle cross-section, with measurements of droplet-substrate angle (left) and metal penetration layer (right).



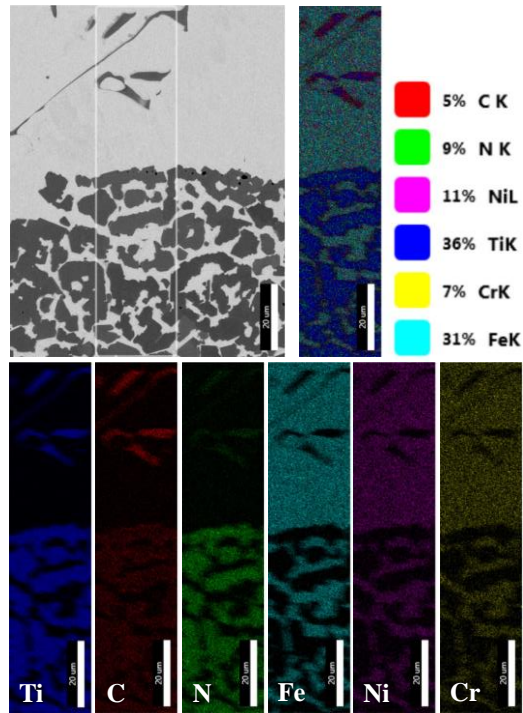


**Figure 7.** Mapping analysis of FeNiCr-Ti(C,N) metal/ceramic region showing elements distribution, where composition is expressed in volume %.

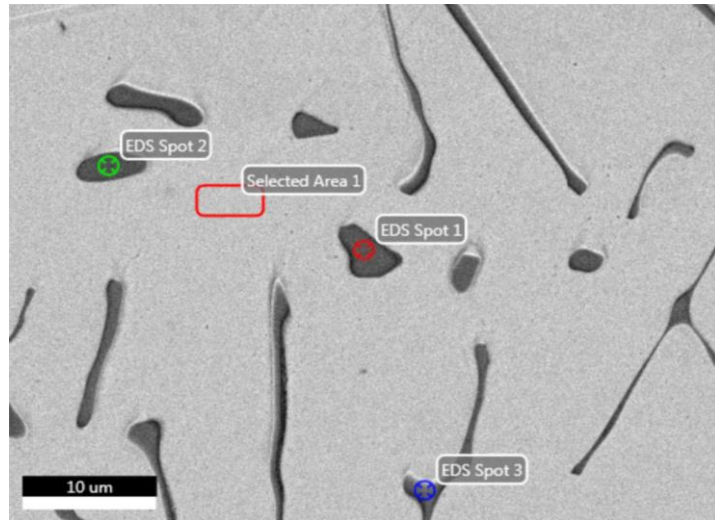


**Figure 8.** FESEM image of the binder region in FeNiCr-Ti(C,N) contact angle, where carbide re-precipitation was observed.

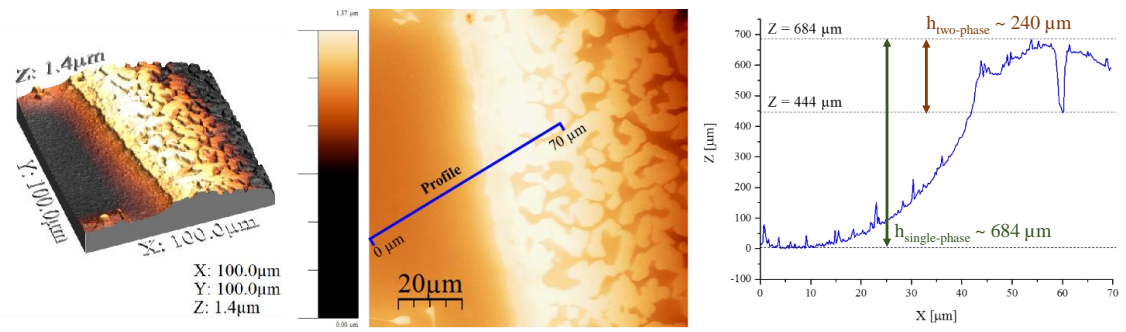


**Figure 9.** AFM 3D-view (left) and topographic (centre) images of FeNiCr-Ti(C,N) contact metal/ceramic region. Profile measurement (right) indicates the height difference between binder/carbide single-phase areas ( $h_{\text{single-phase}}$ ) and binder/carbide at the two-phase zone ( $h_{\text{two-phase}}$ ).

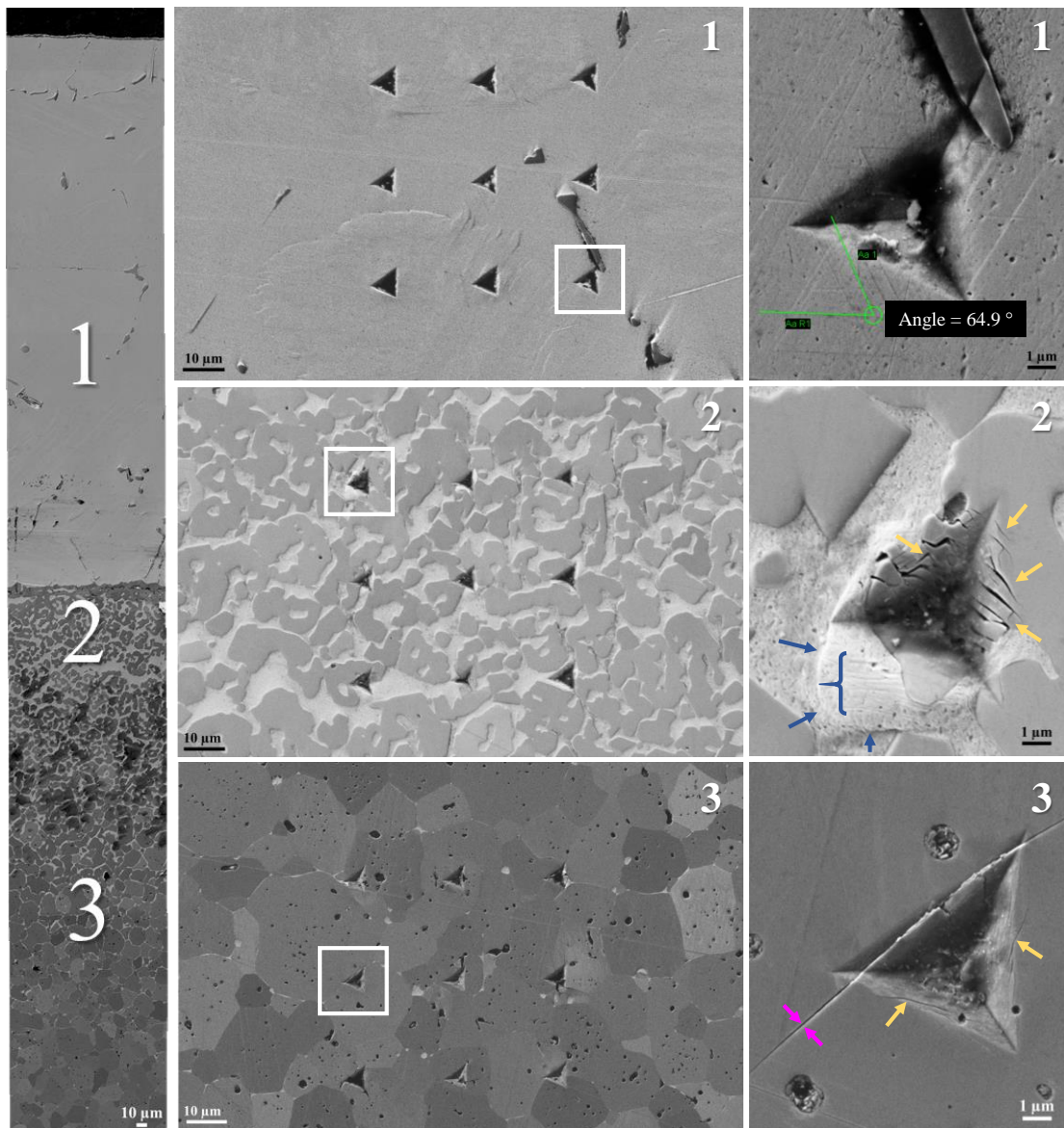


**Figure 10.** Image stitching of FeNiCr-Ti(C,N) contact angle (left), indicating the three areas (1-metal, 2-metal/ceramic, 3-ceramic) where residual nanoindentation imprints could be observed (centre), pointing out special features about each kind (right).



**Figure 11.** Fe<sub>10</sub>Cr<sub>10</sub>Al-Ti(C,N) contact-angle adapted camera pictures taken at different temperatures, showing the no-formation of the metal drop.

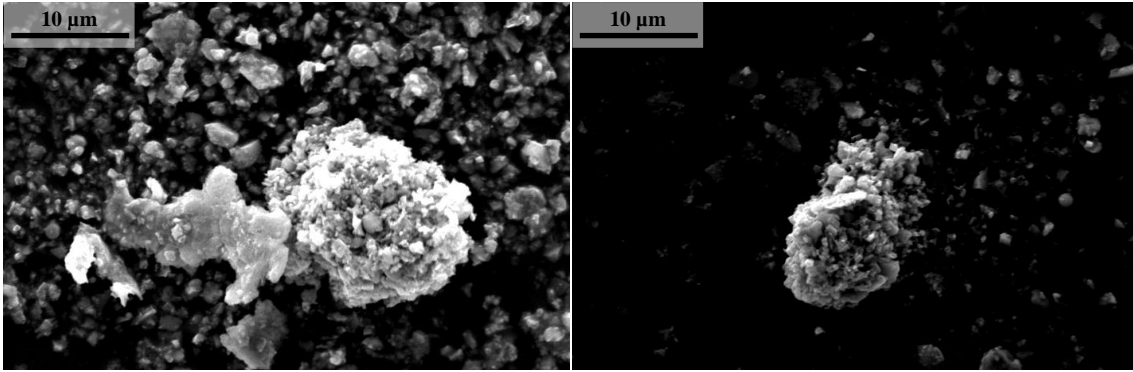


**Figure 12.** SEM images of FeNiCr-Ti(C,N) (left) and FeCrAl-Ti(C,N) (right) mixture powders.

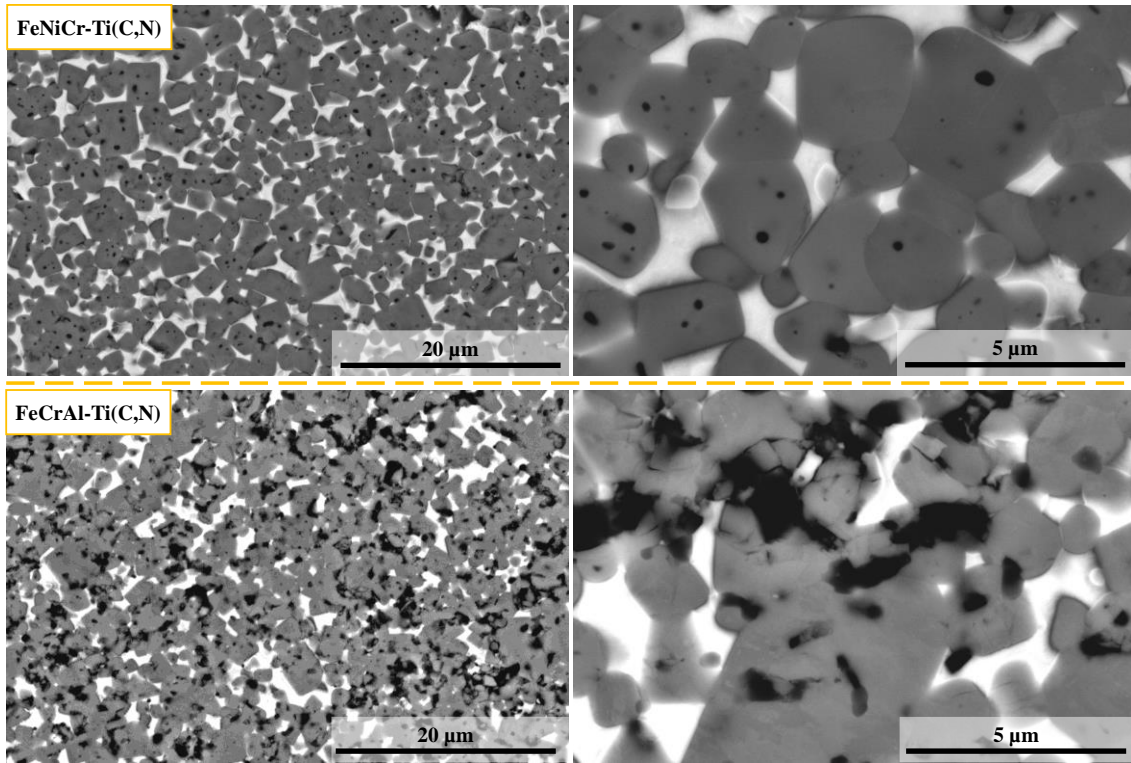


**Figure 13.** FeNiCr-Ti(C,N) (top) and FeCrAl-Ti(C,N) (bottom) FESEM microstructures, at two different magnifications.

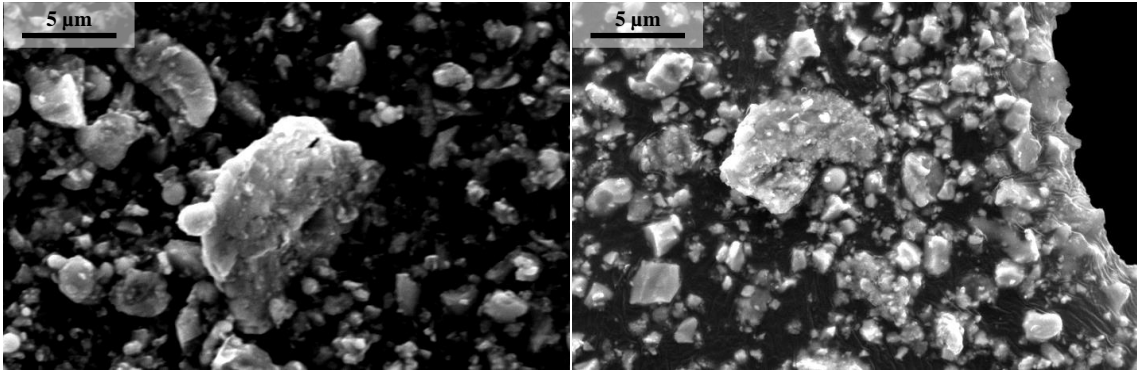


**Figure 14.** SEM images of FeNiCr-Ti(C,N) (left) and FeNiCr-WC (right) mixture powders.



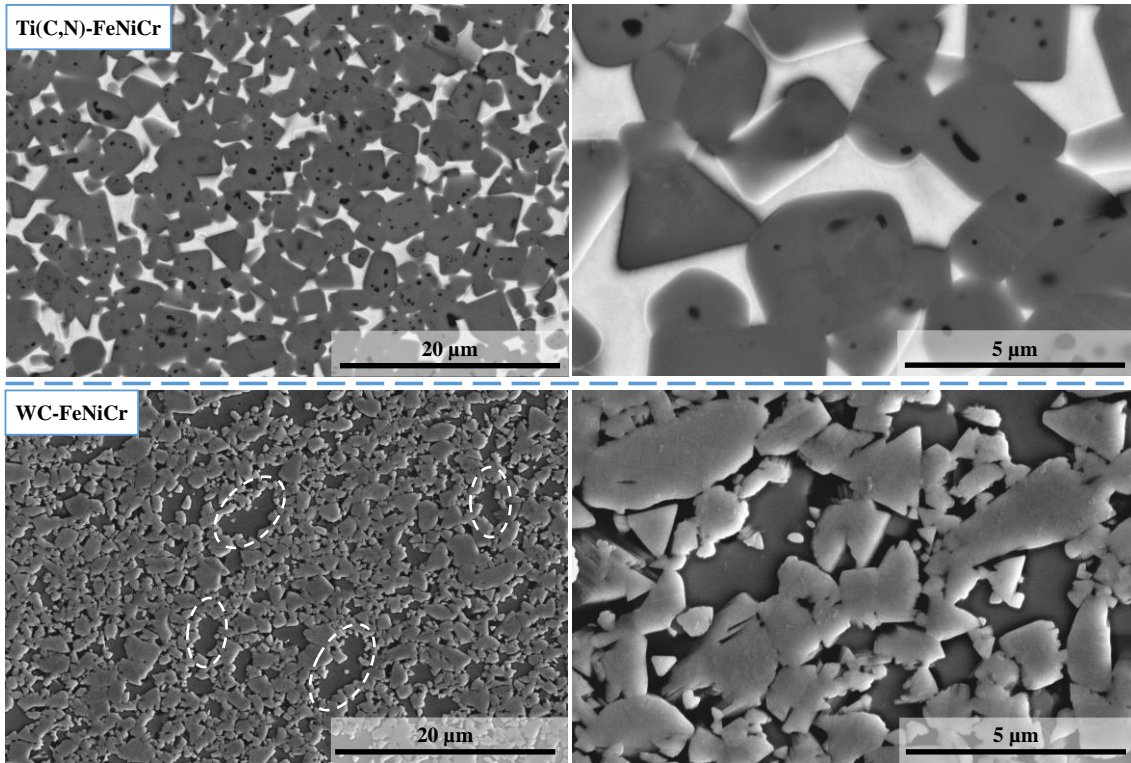


**Figure 15.** FeNiCr-Ti(C,N) (top) and FeNiCr-WC (bottom) FESEM microstructures, at two different magnifications. White-dashed ellipses point out some of the binder pools in WC-FeNiCr composition.

## List of Tables

**Table 1.** Specifications of the as-received commercial powders.

**Table 2.** Compositions of the studied materials.

**Table 3.** Theoretical C content (wt. %) in the hard materials with no extra graphite addition.

**Table 4.** Correlation between simulated (Thermo-Calc®) and experimental (DTA) liquidus temperatures for FeNiCr and FeCrAl alloys without C addition.

**Table 5.** Spots and area EDX analysis at the binder region of FeNiCr-Ti(C,N) contact angle (Figure 8).

**Table 6.** Nanoindentation hardness results obtained at maximum displacement into surface,  $h \sim 1000$  nm.

**Table 7.** Green and sintered relative densities of FeNiCr-Ti(C,N) and FeCrAl-Ti(C,N) materials.

**Table 8.** Green and sintered relative densities of FeNiCr-Ti(C,N) and FeNiCr-WC materials.

**Table 1.** Specifications of the as-received commercial powders.

Powder	Supplier	Characteristics	
		Density *	Size
Ti(C,N) (50/50, grade C)	H. C. Starck (Germany)	$\rho = 5.1 \text{ g/cm}^3$	$D_{50} = 1\text{-}2 \text{ }\mu\text{m}$
WC (040)	Hyperion Materials & Technologies (France)	$\rho = 15.8 \text{ g/cm}^3$	$D_{50} = 2 \text{ }\mu\text{m}$
Fe (SM)	H. C. Starck (Germany)	$\rho = 7.8 \text{ g/cm}^3$	$D_{50} = 3\text{-}4 \text{ }\mu\text{m}$
Ni (UNi-100)	CNPC (China)	$\rho = 8.8 \text{ g/cm}^3$	$D_{50} = 1 \text{ }\mu\text{m}$
Cr	SkySpring Nanomaterials (US)	$\rho = 7.1 \text{ g/cm}^3$	$D_{50} = 5 \text{ }\mu\text{m}$
Al	SkySpring Nanomaterials (US)	$\rho = 2.7 \text{ g/cm}^3$	$D_{50} = 1 \text{ }\mu\text{m}$
Graphite (synthetic, APS)	Alfa Aesar (Germany)	$\rho = 2.3 \text{ g/cm}^3$	$D_{50} = 7\text{-}11 \text{ }\mu\text{m}$
PEG (platelets)	Sigma-Aldrich (Germany)	-	$M_w = 4000 \text{ g/mol}$

\*  $\pm 0.1 \text{ g/cm}^3$  standard deviation

**Table 2.** Compositions of the studied materials.

Comparison method	Material type	Volume %		Weight %	
		Ceramic	Metal	Ceramic	Metal
M1 (binder)	Ti(C,N)-FeCrAl	80	20	75.75	24.25
	Ti(C,N)-FeNiCr			71.97	28.03
M2 (carbide)	Ti(C,N)-FeNiCr	80	20	71.97	28.03
	WC-FeNiCr			88.71	11.29

**Table 3.** Theoretical C content (wt. %) in the hard materials with no extra graphite addition.

Hard materials		Theoretical C content (wt. %)
Binder phase	Ceramic phase	
Fe15Ni10Cr	Ti(C,N)	7.10
	WC	5.44
Fe15Cr10Al	Ti(C,N)	7.48
	WC	5.55

**Table 4.** Correlation between simulated (Thermo-Calc®) and experimental (DTA) liquidus temperatures for FeNiCr and FeCrAl alloys without C addition.

Compositions	Sample type	Liquidus temperatures [°C]	
		Thermo-Calc®	DTA
Fe15Ni10Cr (0 wt. % C)	Powder agglomerate		1491
	Sintered bulk	1476	1492
Fe15Cr10Al (0 wt. % C)	Powder agglomerate		1535
	Sintered bulk	1505	1538

**Table 5.** Spots and area EDX analysis at the binder region of FeNiCr-Ti(C,N) contact angle (**Figure 8**).

Element	Spot 1	Spot 2	Spot 3	Area 1
Ti	40.72	2.75	1.97	2.18
C	54.19	26.15	22.80	21.40
N	3.74	-	-	-
Fe	1.03	54.60	58.01	58.72
Ni	-	9.56	10.04	10.20
Cr	0.32	6.94	7.19	7.50
Total at. %	100	100	100	100

**Table 6.** Nanoindentation hardness results obtained at maximum displacement into surface,  $h \sim 1000$  nm.

Region	Hardness (GPa)
Metal (1)	$7.44 \pm 1.38$
Metal/ceramic (2)	$22.26 \pm 11.18$
Ceramic (3)	$42.11 \pm 3.94$



**Table 7.** Green and sintered relative densities of FeNiCr-Ti(C,N) and FeCrAl-Ti(C,N) materials.

Material	Green relative density [%]	Sintered relative density [%]
FeNiCr-Ti(C,N)	$64.59 \pm 0.13$	$97.09 \pm 0.39$
FeCrAl-Ti(C,N)	$65.92 \pm 0.52$	$89.37 \pm 0.40$

**Table 8.** Green and sintered relative densities of FeNiCr-Ti(C,N) and FeNiCr-WC materials.

Material	Green relative density [%]	Sintered relative density [%]
FeNiCr-Ti(C,N)	$66.23 \pm 0.26$	$95.23 \pm 0.32$
FeNiCr-WC	$61.43 \pm 0.73$	$91.95 \pm 0.43$